Magnetohydrodynamic Modeling of Interplanetary CMEs

Pete Riley, J. A. Linker, Z. Mikic
Science Applications International Corporation
10260 Campus Point Dr.
San Diego, California 92121, USA
Email: Pete.Riley@saic.com; Jon.Linker@saic.com; Zoran.Mikic@saic.com

Dusan Odstrcil
NOAA, Space Environment Center
325 Broadway
Boulder, Colorado 80305, USA
Email: Dusan.Odstrcil@noaa.gov

***Abstract*— Heliospheric models of Coronal Mass Ejection (CME) propagation and evolution provide an important insight into the dynamics of CMEs and are a valuable tool for interpretating interplanetary in situ observations. Moreover, they represent a virtual laboratory for exploring conditions and regions of space that are not conveniently or currently accessible by spacecraft. In this report we summarize our recent advances in modeling the properties and evolution of CMEs in the solar wind. We describe our current state of research with three examples: (1) Interpreting the global context of in situ observations; (2) Identifying new phenomena in the simulations; and (3) computing geo-effective phenomena. We conclude by discussing what topics will likely be important for models to address in the future.**

I. Introduction

The disruption of magnetically closed regions in the solar corona often leads to the eruption of large quantities of material into interplanetary space. During these events, known as coronal mass ejections (CMEs), $10^{12} - 10^{13}$ Kg of material are typically released. CMEs play a crucial role in the large-scale evolution of the solar corona (e.g., [1]) and are the leading cause of large, non-recurrent geomagnetic storms (e.g., [2]) Fast CMEs, in particular, have been identified as the leading cause of non-recurrent geomagnetic storms [3] and can also enhance the geoeffectiveness of recurrent storms [4], making their study of practical importance.

While the coronal magnetic field is undoubtedly the source of energy for the eruption of a CME at the Sun, the basic preeruption configuration and the topological changes in the magnetic field that result in the conversion of magnetic energy into kinetic energy are not well known. By necessity, modeling efforts must be idealized and as such tend to focus on reproducing a particular aspect of the eruption process at the expense of others. While analytic and numerical models have been successful in two dimensions, we are only now beginning to explore the additional richness and complexity that the third dimension brings. Given the inherent complexity of CMEs, it is hardly surprising that theoretical models tend to be idealized. Nevertheless, if we are to make progress in understanding such phenomena, it is important to make connections between models and observations.

Simulations of CME evolution in the inner heliosphere have typically started at 20 – 30 solar radii (R_S) from which point it is both computationally and physically a much simpler problem to solve. Unfortunately, there are little to no observable parameters at these distances to constrain the boundary conditions, which can lead to a game of "tweaking", where you modify your boundary conditions to improve fits to the observations; all without fear of contradicting any observable parameter [5]–[9]. More recently, modelers have extended the lower radial boundary to $1R_S$, but have included ad hoc eruptions, such as superimposed density enhancements [10] or analytic flux rope representations [11]. In these cases, a CME is driven by the resulting force imbalance. In contrast, the approach we have taken is to model the entire process from CME initiation – using a mechanism that is consistent with observations, although not necessarily correct – through its evolution in the inner heliosphere. Our lower boundary is the photosphere, which is a readily observable region. We use either idealized magnetic field configurations or observed line of sight observations of the photospheric magnetic field.

Using a global resistive MHD model, we have been able to reproduce many of the observed features of coronal mass ejections in the corona and solar wind. Moreover, the simulation results have predicted features that we believe have been subsequently identified in the observations. While these simulations are currently research tools, we expect that in the near future, they will be capable of predicting potentially geo-effective phenomena in the near-Earth environment.

In this report we summarize our recent advances in modeling the properties and evolution of CMEs in the solar wind. We focus on the physics described by our models rather than the models themselves. We summarize our current state of research with three applications of the models, and we suggest what topics will likely be important for models to address in the future.

II. Description of the Model

In this section we briefly describe the basic features of the coronal and heliospheric models and discuss their integration. A more detailed description is provided elsewhere [12]. We solve the basic set of time-dependent, magnetohydrodynamic (MHD) equations that describe many aspects of the large-scale behavior of the solar corona and inner heliosphere. We separate space into two parts, distinguishing between the "coronal" region, which spans the photosphere up to 20 R_S,

and the "heliospheric" region, which spans 20 R_S to 5 AU. The SAIC coronal MHD model [13] is used to solve for the coronal region and the NOAA/SEC heliosperic MHD model [8] is used to solve for the heliospheric region, being driven directly by output from the coronal solution. This appoach has a number of practical and scientific advantanges. In particular, each code has been designed specifically for its respective environment. Moreover, decoupling these regions in this way allows the heliospheric portion to run at significantly larger time steps than are required by the coronal algorithm.

The details of the algorithm used to advance the equations of the SAIC coronal model are given elsewhere [13]–[15]. Here we make a few brief remarks. The equations are solved on a spherical (r, θ, ϕ) grid, which permits non-uniform spacing of mesh points in both r and θ, thus providing better resolution of narrow structures, such as current sheets. In the radial (r) and meridional (θ) directions we use a finite-difference approach. In azimuth (ϕ), the derivatives are calculated pseudo-spectrally. We impose staggered meshes in r and θ, which has the effect of preserving $\nabla \cdot \mathbf{B} = \mathbf{0}$ to within round-off errors for the duration of the simulation.

The NOAA/SEC heliospheric model solves the time-dependent MHD equations in a spherical geometry using either the Flux-Corrected-Transport or Total-Variation-Diminishing schemes (e.g., [16], [17]). These high-resolution schemes produce second-order accuracy away from discontinuities, while simultaneously providing the stability that ensures non-oscillatory solutions.

The SAIC coronal model, as implemented here, uses a polytropic index of $\gamma = 1.05$ to mimic the near isothermal nature of the solar corona, and thus produces plasma parameters that agree with observed values. On the other hand, the NOAA/SEC code uses $\gamma = 5/3$ in agreement with the observed near adiabatic nature of the solar wind. Ideally one would like to implement a coronal model incorporating conduction, coronal heating, radiation loss, and Alfvén wave acceleration, together with $\gamma = 3/2$ to provide a seamless boundary between the two models. Unfortunately, practically speaking, such an approach is only now becoming feasible in two dimensions [18]. We have examined solutions in the vicinity of the boundary between the two models to estimate what artifacts may have been introduced by allowing γ to vary discontinuously across the boundary. Remarkably, with the exception of temperature (and hence thermal pressure), the magnetofluid parameters remain continuous. The plasma temperature profile with radial distance obviously changes abruptly at the boundary since $T \propto r^{-2(\gamma-1)}$. Thus in the coronal model, $T \propto r^{-1/10}$, whereas in the heliospheric model, $T \propto r^{-4/3}$. We are currently exploring improvements to the solar model to remove this artifcat. Nevertheless, our analysis suggests that the results are qualitatively correct.

For the results presented here, the coronal solution was computed on a non-uniform grid of 200×300 points. The radial spacing ranged from $0.005 R_S$ at the inner boundary ($1 R_S$) to $0.6 R_S$ at the outer boundary. The latitudinal spacing ranged from $0.24°$ to $2.4°$, with the finest resolution located in the streamer belt. In contrast, the heliospheric solution was computed on a uniform grid with a radial spacing of $0.6 R_S$ and a meridional spacing of $0.5°$.

III. Flux Eruption at the Sun

The configuration of the solar corona prior to the emergence of a flux rope is summarized in the two left-most panels of Figure 1. This type of equilibrium solution has been discussed in more detail elsewhere [19]. Contours of the magnetic flux function (fiduciaries of magnetic field lines in two dimensions) are shown by the shaded contours (top). The system consists of a single streamer belt displaced $\sim 10°$ below the heliographic equator. In the bottom panel, we show the simulated polarized brightness (pB). This was constructed by integrating the product of the number density with scattering function [20] along the line of sight. The resulting image bears a strong generic resemblance to SOHO/LASCO white-light images taken near solar minimum. The first column shows the state of the corona after the system has reached equilibrium. The second column shows how this configuration is modified via photospheric shear of the field line foot points [21]. At this point, the system is still in equilibrium.

In our idealized system, the asymptotic wind speed is the same at all heliographic latitudes. In reality even the "steady" solar wind is more complex than this. At solar minimum, large polar coronal holes produce uniform high-speed wind at higher latitudes, whereas interaction regions (formed from the interaction of slow and fast streams) at low- and mid-latitudes produce a slower and more variable wind. At solar maximum, on the other hand, smaller, mid-latitude or equatorial coronal holes produce intermediate, more variable speeds within relatively small volumes of the heliosphere, and slow and variable wind occupies the majority of space (e.g., [22]). The interaction of a flux rope with a more realistic ambient wind requires a three-dimensional treatment and will be the topic of a future study.

Theories of flux rope CMEs generally start from the premise that CMEs are initiated by the release of energy stored in the coronal magnetic field [23]. Previously, we have studied the possibility that eruptions could be initiated by photospheric motions that shear and twist the coronal magnetic field [13], [21], [24], [25]. These studies indicate that when the magnetic field is sheared beyond a critical value, helmet streamer configurations can erupt in a manner similar to "slow" CMEs, i.e., coronal mass ejections that are carried out of the corona by the solar wind. It has proven difficult to demonstrate that enough energy can be released rapidly enough by this mechanism to produce a "fast" CME that can drive an interplanetary shock. A more promising mechanism for producing fast CMEs is magnetic flux cancellation. We have found that a reduction in the magnetic flux (i.e., flux cancellation) near the neutral line of a sheared or twisted arcade configuration (such as that in the second column of Figure 1) can lead to the formation of magnetic flux ropes [26]–[28]. When the flux cancellation reaches a critical threshold, the entire configuration erupts with the release of a considerable amount of magnetic energy.

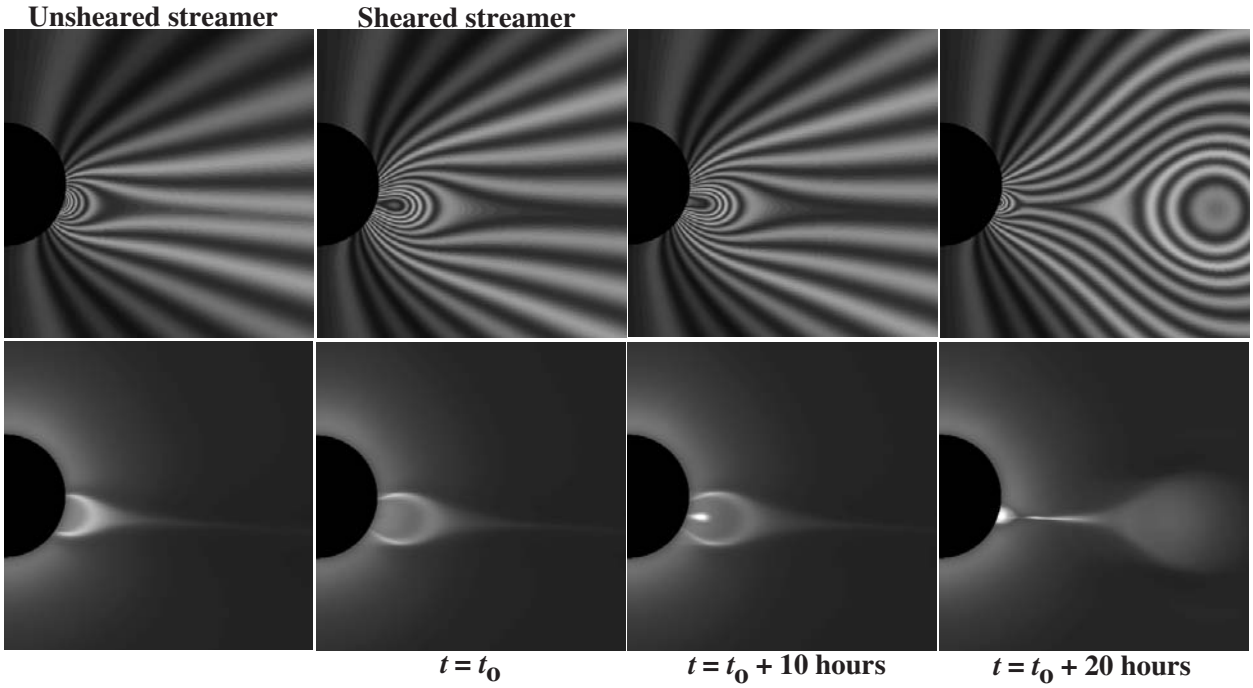

Fig. 1. Evolution of a sheared helmet streamer via flux cancellation. Top panels show contours of the magnetic flux function, which in two dimensions are equivalent to the magnetic field. Bottom panels show simulated polarized brightness. The four columns summarize: (1) the state of the unsheared corona; (2) the sheared corona; (3) the eruption of a flux rope at 10 hours following the cancellation of flux; and (4) the eruption of the flux rope after 20 hours, respectively.

The remaining two columns of Figure 1 show the launch of just such a flux rope at 10 hrs and 20 hrs following the cancellation of flux. As can be seen, the origins of the the flux rope lie in the closed magnetic field lines embedded within the streamer belt. As the flux rope erupts into the solar corona, overlying field lines, which are still connected back to the Sun at both ends, are brought together under the flux rope. As they reconnect with each other, they contribute both to the flux of the evolving flux rope to the right of the reconnection site and to the re-growth of the streamer belt to the left. Note that the flux rope develops an elliptical shape, with its major axis approximately horizontal. Note also that the reconnection site underneath the erupting flux rope is visible in the simulated pB image at $t = 20$ hours. This density enhancement was produced by the transverse (i.e., approximately parallel to the solar surface) flow of plasma into the reconnection region and has been observed in white light images [29].

With regard to the simulated polarized brightness images, we also remark that they bear a strong resemblance to the classic three-part structure of CMEs observed in white light. Specifically, the bright front, dark cavity, and dense core. Since this simulation was based on a polytropic approximation to the energy equation, associating the bright core with prominence material is, strictly speaking, not applicable. Nevertheless, when similar simulations, incorporating more realistic thermodynamics are run, the formation of a prominence is clearly produced [28].

IV. ICME Evolution

The plasma and magnetic field parameters from the outer boundary of the coronal simulation are used to drive the inner boundary of the heliospheric solution at 20 R_S. Figure 2 illustrates the evolution of the flux rope and its associated distubances at 6 distances between the Sun and 1 AU. In this display we have combined results from both models. The boundary between the two models is indicated by the thick white line at $20R_S$: No obvious discontinuities are apparent. Note that the coronal model spans all latitudes while the heliospheric model covers $\pm 60°$. We have analyzed the continuity of the solution at this interface in detail, concluding that no significant artifacts are introduced [12]. We note the following features from the Figure. First, the initially elliptical flux rope becomes circular and then develops into a "pancake" structure. This is a combination of: (1) kinematic expansion, as the ejecta moves into an ever larger spherical volume; and (2) dynamic evolution as the ejecta plows into slower ambient solar wind ahead. Second, a fast forward shock, driven by the ejecta, propagates poleward to the boundary of the calculation ($\pm 60°$ heliographic latitude). Third, both the shock and flux rope are beginning to develop concave-outward deformations in the vicinity of the plasma sheet, as they propagate through the denser medium [30].

Figure 3 shows the evolution of the ejecta and its associated disturbance between 1 AU and 5 AU. We have restricted the range in displayed speeds to 390-490 km s^{-1} to emphasize flows associated with the disturbance. Note how the ejecta

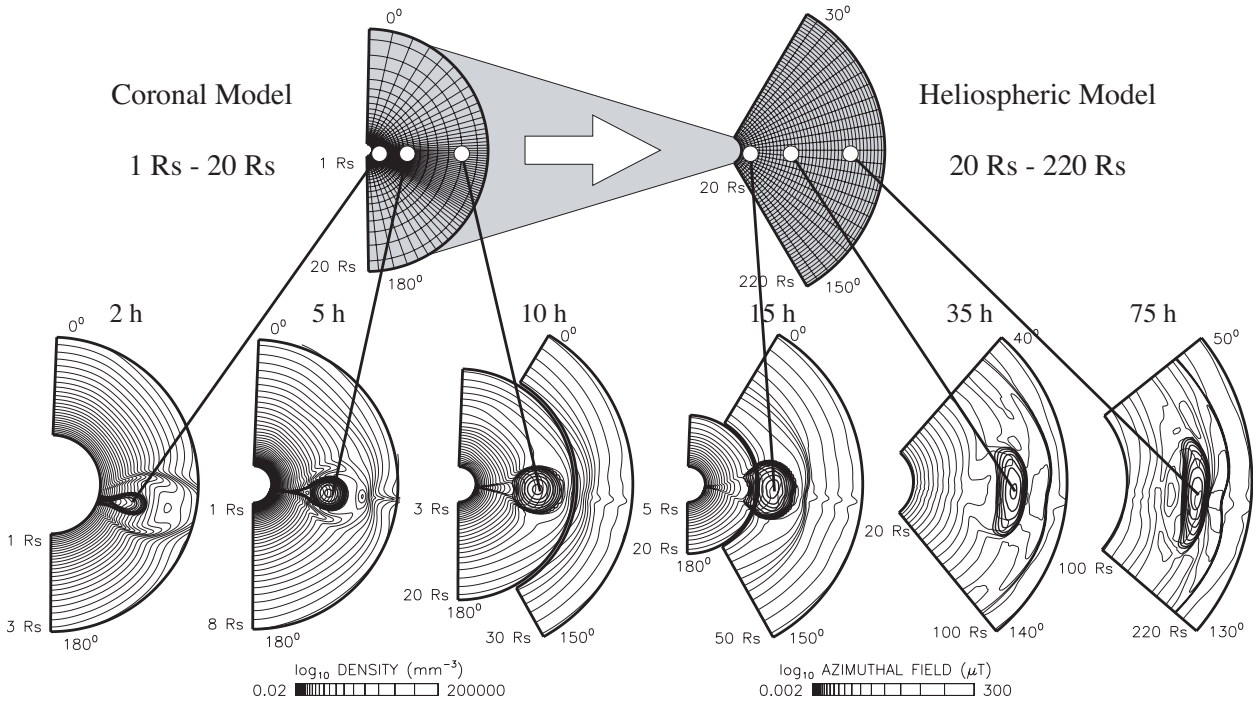

Fig. 2. Evolution of a flux rope through the solar corona to $\sim$ 1 AU. (Top) Illustration of the merging of the coronal and heliospheric models. (Bottom) Density and azimuthal field at 6 times following the eruption. The interface between the coronal and heliospheric model is marked by the thick black line.

becomes progressively more distorted with increasing heliocentric distance. By ~ 5 AU it has been squeezed so much at low latitudes that it has evolved into two lobes, connected by a thin band of compressed field. A detailed study of this aspect will be presented elsewhere. We can also identify enhanced outflow associated with post-eruption reconnection underneath the flux rope, which has remained intact within the expansion wave (rarefaction region) behind the flux rope. This aspect of the simulation is discussed in more detail below.

An interesting, but relatively misunderstood, phenomenon is the pancaking of the ejecta as it moves away from the Sun. It has typically been interpreted as the result of the fast ejecta ploughing into slower ambient wind and becoming compressed. While this effect undoubtedly makes a contribution, the distortion is dominated by a much simpler kinematic process, related to the spherical expansion of the solar wind. In fact it is straightforward to show that an initially circular cross section that simply convects outward with the ambient solar wind will develop such a convex-outward shape [31]. Thus the idea that CMEs have cylindrical cross sections at 1 AU is not realistic, even as a 1st approximation.

Although the 2-D simulation we have just described is remarkably rich in content, it suffers from a number of limitations. Perhaps most importantly is in regard to field line connectivity. In two dimensions, the topology of the field lines is very simple. Moreover, an erupting flux rope in 2-D is really a torus, encircling the Sun such that all of the helical field lines within the ejecta are disconnected from the Sun. Yet we know, from observations of suprathermal counterstreaming electrons, that field lines within CMEs typically are connected back to the Sun at both ends [32].

In three dimensions, we can model an eruption where the footpoints of the flux rope remain tied to the Sun as the ejecta propagates away from the Sun. Because of this, the pattern of magnetic reconnection can be much more complicated and a variety of topologies can be produced [33]. Figure 4 shows a global perspective of a simple 3-D simulation that illustrates this. The meshed-surface is an isosurface of density, scaled by $r(AU)^2$ to account for the spherical expansion of the solar wind. Given the large azimuthal extent of the ejecta, one can see that this is a large-scale eruption. In fact, it is currently a challenge to simulate an eruption that is limited in longitude. The relatively flat isosurface marks the location of the heliospheric plasma sheet. The inner sphere marks the boundary between the coronal and heliospheric model, in this case $30R_S$. The outer boundary is at $230R_S$, just beyond 1 AU ($\sim 215R_S$). A selection of field lines has been drawn to indicate various topologies: helical field lines that define the flux rope; open field lines that are connected to the Sun at one end; and field lines that are completely disconnected from the Sun, as a result of the eruption of the flux rope.

The topology of these field lines is important for the propagation of energetic particles. For example, the corona is a continuous source of suprathermal electrons. Typically, a single beam of such particles is seen on ambient solar wind field lines. During the passage of a CME, however, we observe suprathermal electrons in both directions, indicating that the field lines are connected to the Sun at both ends. Occasionally no suprathermals are seen. These intervals are presumably the result of reconnection leading to the disconnected field lines

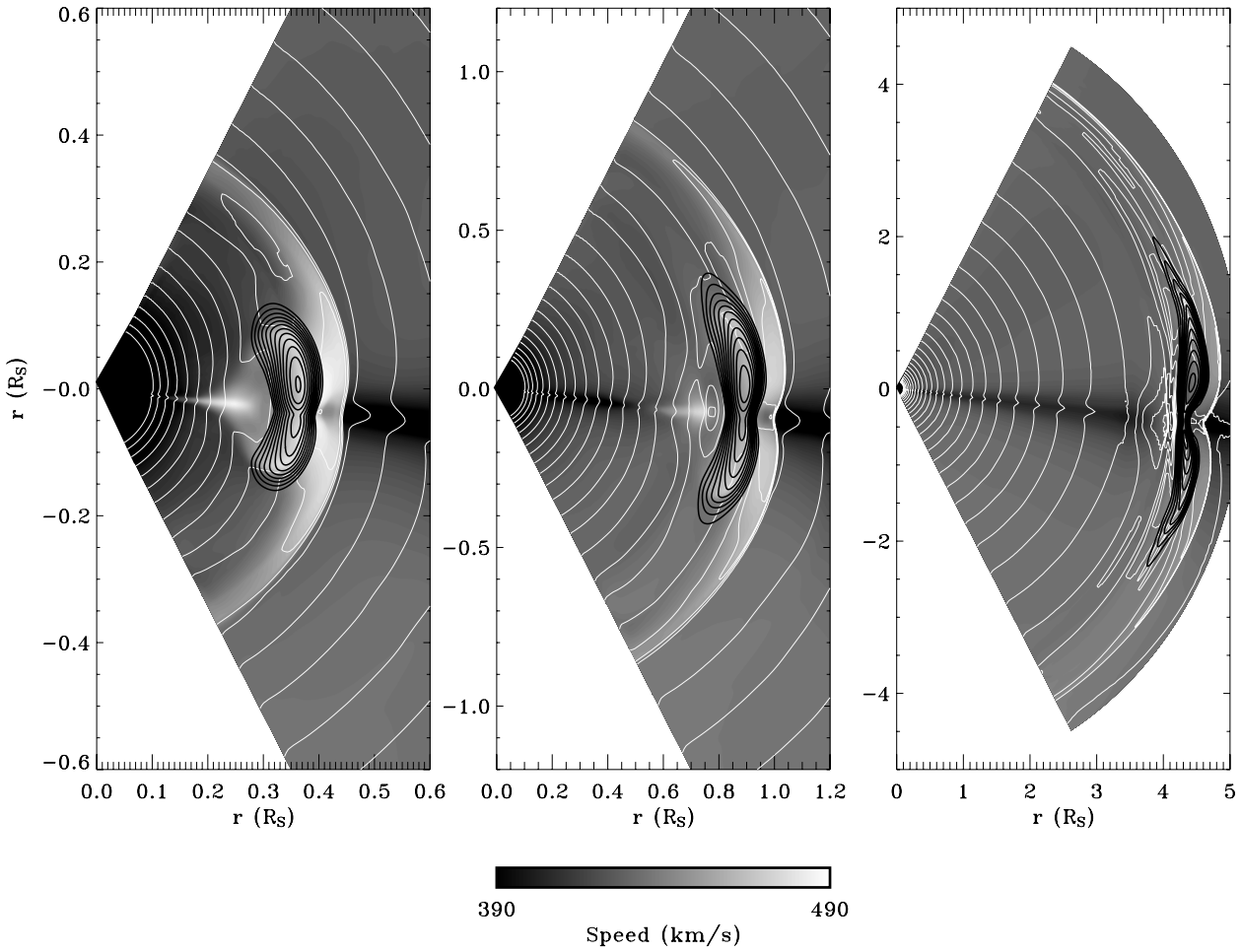

Fig. 3. Evolution of the flux rope in the inner heliosphere. The panels extend ± 60 ° in latitude and from left to right, extend in heliocentric distance from the Sun to: 0.6 AU, 1.2 AU, and 5 AU. The contours denote: radial velocity (grey shading); density (grey lines); and magnetic field (black lines).

(e.g., [33]).

V. Model Applications

To illustrate the value of these calculations, we summarize three applications of these types of simulations. Specifically, we use the model results to: (1) Interpret the global context of in situ observations; (2) Identify new phenomena that can be recognized in the data; and (3) Predict geo-effective phenomena.

A. Comparison with In Situ Observations

In late February, 1999 the ACE spacecraft observed a flux-rope CME lasting for 21 hours. Thirteen days later Ulysses observed a flux-rope CME that lasted for 50 hours [34]. At this time ACE was located at a heliocentric distance of 1 AU, very close to the ecliptic plane, while Ulysses was located at $22°S$, 5 AU from the Sun, and at approximately the same heliolongitude as ACE. Although the plasma and magnetic profiles of these events were quite dissimilar, it has been argued that: (1) the lack of more than one source at the Sun; (2) the longitudinal alignments; (3) the rotational orientations of the magnetic fields; and (4) the average transit speed to both

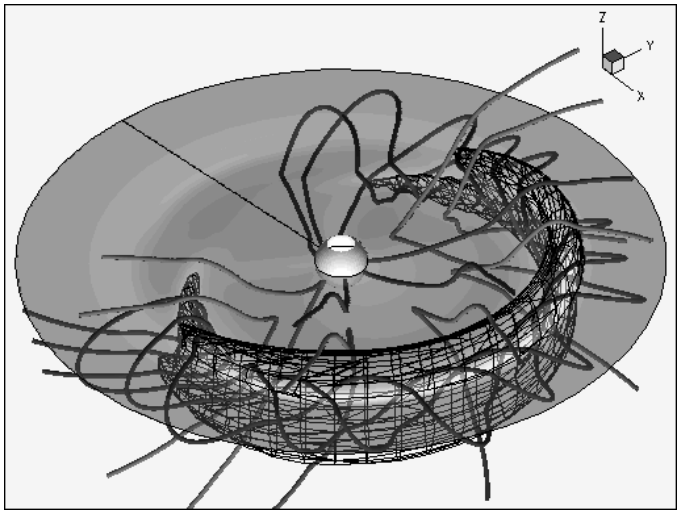

Fig. 4. Summary of CME eruption in three dimensions. The meshed surface is an isosurface of density (scaled by r^2) and the solid grey isosurface marks the location of the HCS. A selection of field lines have been drawn to highlight a range of topologies: (1) closed field lines; (2) open field lines; and (3) disconnected field lines.

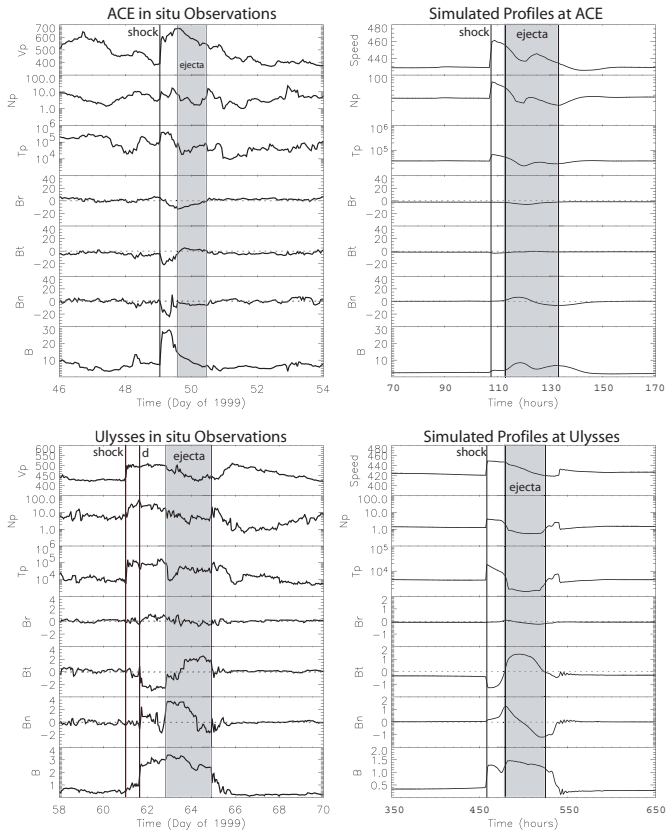

Fig. 5. Comparison of observed plasma and magnetic field parameters (left) with simulated parameters (right).

spacecraft support the conclusion that these were the same event [34] .

By flying the ACE and Ulysses trajectories through the simulation results summarized by Figures 1-3 we can make direct comparisons with the in situ observations. We reiterate that this is a generic simulation and not constructed to mimic any specific event quantitatively. We believe, however, that it contains the basic qualitative features of many CMEs in the solar wind. In Figure 5 we compare speed, proton density and temperature, magnetic field strength and directions from ACE (top left) and Ulysses (bottom left), with simulation results (top right and bottom right, respectively). Based on force-free fittings at the two spacecraft [35], we infer that ACE intercepted the CME near its flank, whereas Ulysses intercepted it closer to the axis, suggesting that the centroid of the CME was displaced significantly southward of the equator. In our simulation, however, the axis of the CME was displaced southward by a modest $\sim 10°$. Thus to make more meaningful comparisons with the observations, we extracted ACE profiles at $18° N$ and Ulysses profiles at $2° N$. In essence, then, we have reversed the relative latitudinal positions of the spacecraft in the simulation.

Comparison of the simulation results with the in situ observations reveals a number of similarities, yet the generic nature of the model also necessarily leads to a number of discrepancies. We focus first on the observed variables at ACE. The ejecta was traveling significantly faster than the ambient solar wind ($\sim$ 590 km s^{-1} vs. $\sim$ 400 km s^{-1} at 1 AU) and drove a relatively strong shock. The proton density and temperature profiles did not show large dips within the ejecta, typically indicative of expansion. The magnetic field within the ejecta showed little systematic variation. Of some note, however, is the small rotation in the radial component of the field. The magnetic field strength decreased from the leading edge to the trailing edge and was maximum in the sheath region preceding the ejecta; both aspects resulting from the fast speed of the ejecta relative to the ambient solar wind. The simulation results mimic the speed profile fairly well. This would be expected, since any expanding ejecta traveling faster than the ambient solar wind ahead and behind will drive a wave/shock ahead and present a decreasing speed profile within the ejecta. The temperature, density, and field component profiles do not have any definitive features that we can associate with the observations. Finally, the magnetic field magnitude, while enhanced within the ejecta, does not have the characteristic peak in the sheath region. As we have noted, this is likely due to a lower velocity difference between ejecta and ambient wind ahead in the simulations.

At Ulysses, the ejecta is inferred to be expanding, and presumably driving the shock at the beginning of day 61. This basic profile is mimicked in the simulation results. Note that the observed shock boundary is distinct from the magnetic discontinuity (marked 'd') later on day 61 and suggests that the interaction between the ejecta and the ambient solar wind was more complex than the simpler picture suggested by the simulation. Turning to a comparison of the magnetic field vectors, we note that the large-scale rotations in all components are mimicked well by the simulations. In particular: (1) the flat B_r profile; (2) the rise and fall in B_t; and (3) the rotation from positive to negative values in B_n. Finally, the magnetic field strength compares quite favorably, with a relatively flat (or slightly falling) profile within the ejecta, and more rapid fall off behind. Comparison of either the observed or simulated magnetic field strength profiles at the two spacecraft suggests that this was a strongly magnetic structure at Ulysses, but less so at ACE.

B. Identification of New Phenomena

In addition to reproducing many generic features of flux rope CMEs (or magnetic clouds), these simulations can be used to identify new phenomena, which can then be searched for in the data. This may serve to place additional contraints on the models and may even differentiate between competing mechanisms. As an example, we report on one such phenomena: the possible evidence of post-eruption reconnection associated with coronal mass ejections in the solar wind [36].

Figure 6 shows the reconnection site underneath the erupting CME of Figure 1 in more detail. The left panel shows magnetic field lines (solid lines), flow vectors (arrows) and the ϕ component of the current density (J_ϕ) at ~ 20 hours following the eruption onset. The site of reconnection is clearly visible as the sharp increase in current density near the equatorial

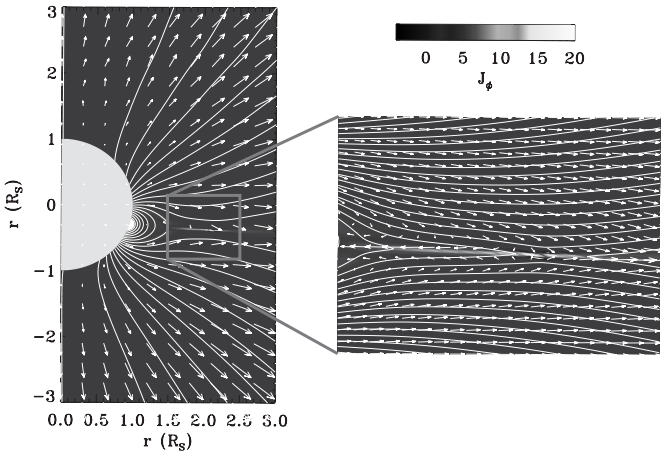

Fig. 6. Evolution of X-type neutral line underneath the erupting flux rope. Field lines are shown as solid lines, arrows mark the velocity vectors, and the grey contours represent the current density in the azimuthal direction (J_ϕ).

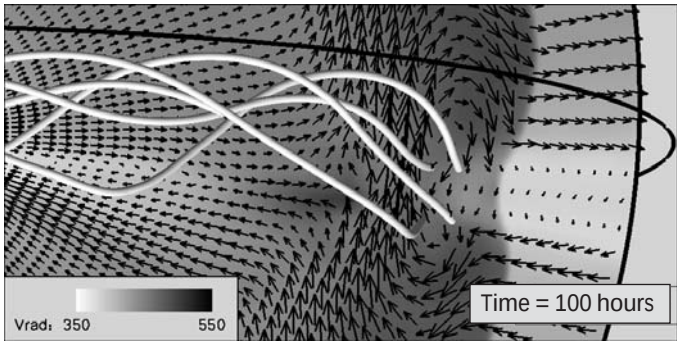

Fig. 7. Detailed view of the magnetic flux rope. In the meridional plane the flow velocity (km/s) is shown by the grey contours, while the magnetic field is shown as vectors. Selected magnetic field lines embedded within the flux rope are shown extending out of the meridional plane. The black, roughly horizontal line marks the location of the equatorial plane.

plane. The panel on the right shows this region in more detail. The flow pattern is generally directed away from the Sun but develops a significant meridional component near the extended X-type neutral point. In a frame convecting with the ambient solar wind, this flow pattern would have the more familiar vertical inflow, such as described by Sweet [37], [38], Parker [39] and Petschek [40]. The reconnected outflow does flow away from the X-point in both directions. To the left, it is associated with the rebuilding of the streamer belt and to the right, it flows away from the Sun, behind the ejected flux rope. Note that in this scenario, the plasma populating the new streamer belt came, at least initially, from the reconnected outflow, which in turn had its origins in fast solar wind associated with coronal hole flow.

Figure 7 shows a detailed meridional view of the flux rope as it approaches 1 AU. The flow velocity is indicated by the grey contours and the magnetic field is indicated by vectors. A selection of magnetic field lines that thread the ejecta are shown extending out of the meridional plane. Earth's orbit is shown by the solid black line. Of particular relevance here is the velocity enhancement that can be seen behind the ejecta. This enhanced outflow is associated with the post-eruption reconnection and has remained intact within the expansion wave (rarefaction region) behind the flux rope. It has a limited latitudinal extent ($\pm 15^\circ$) and trails the ejecta by $\sim 35 R_S$ (0.16 AU) at 1 AU.

Given the small angular extent of the reconnection outflow, one might expect to observe such a phenomena only rarely. Moreover, to maintain such a structure out to 1 AU requires a quiescent medium within which to propagate, such as the expansion wave that follows the fast ejecta in our model calculation. We have found several examples of magnetic clouds in the literature that bear striking similarities with the model results, suggesting that indeed such a phenomena has been observed. For the purposes of illustration, we study one of the very first reported observations of a magnetic cloud; the February 11, 1968 event [41]. The observations are shown in Figure 8 (left panels) where they are compared with the simulation results (right panels). Focusing first on the observations, we note that this typical flux rope is moving faster than the ambient solar wind and driving a fast-mode forward shock ahead of it. Within the flux rope, the density and temperature are depressed while the magnetic field is enhanced. Large coherent rotations were present in all three components of the field (not shown). The simulation results show these same basic variations. The lack of an appreciable magnetic field strength in the sheath region (i.e., between the flux rope and the shock wave) can be attributed to the neglect of solar rotation, which would produce azimuthal fields that could then be compressed by the ejecta (this simulation was a simplified version of that summarized in Figures 1, 2, 3, and 5 and did include solar rotation). Following both the observed and simulated ejecta is a speed enhancement, lasting $\sim 3/4$ day. The observed velocity pulse has an amplitude of ~ 60 km s^{-1} above ambient solar wind values, while the simulation peaks at ~ 30 km s^{-1}.

This event has been studied within the approximation of force-free models. Marubashi [42] computed the latitudinal and longitudinal angles of the axial magnetic field to be $\theta = -10.9^\circ$ and $\phi = 238^\circ$, respectively, indicating that the flux rope was oriented predominantly in the equatorial plane and obliquely to the radial direction. These values should be viewed with some caution, however, as Lepping et al. [43] found values of $\theta = -29^\circ$ and $\phi = 252^\circ$ using a similar fitting technique. More relevant to the present study, Marubashi and Lepping et al. computed impact parameters (i.e., the distance of closed approach to the axis of the flux rope in units of the flux rope radius) of 0.32 and 0.51, respectively. Thus the spacecraft apparently did not intercept the flux rope head on, as would have been predicted given the geometric constraints suggested by the simulation.

Should these results be substantiated further, they may allow us to distinguish between competing theories of CME models. In particular, the "breakout" model [44], which predicts reconnection to occur above the flux rope, would not be reconcilable with these observations. Of course, given that the

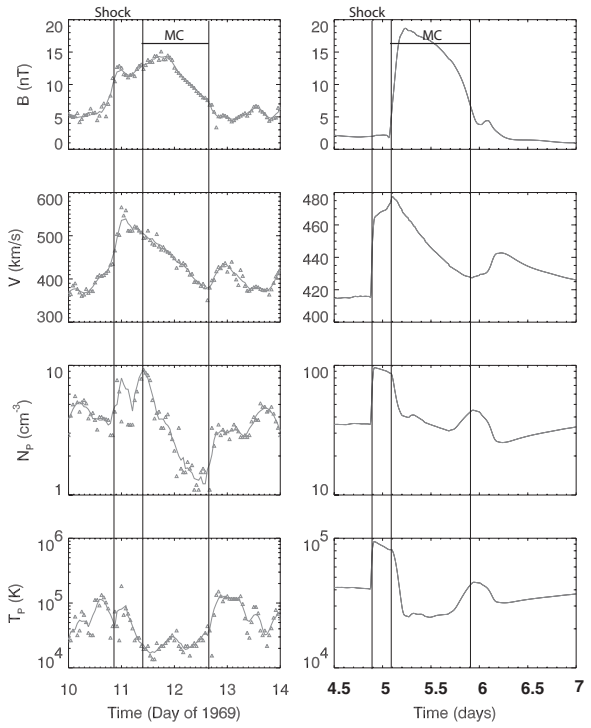

Fig. 8. Comparison of in situ measurements (left) of magnetic field strength (B), flow speed (V), proton number density (N_p), and proton temperature (T_p) with simulation results (right). Vertical lines mark the inferred location of the magnetic cloud (flux rope) and the shock preceding it. For the left panels, the triangles show 1-hour averaged data whereas the solid line has been box-car averaged over 5 points. For the right panels, the time is measured since the onset of the eruption.

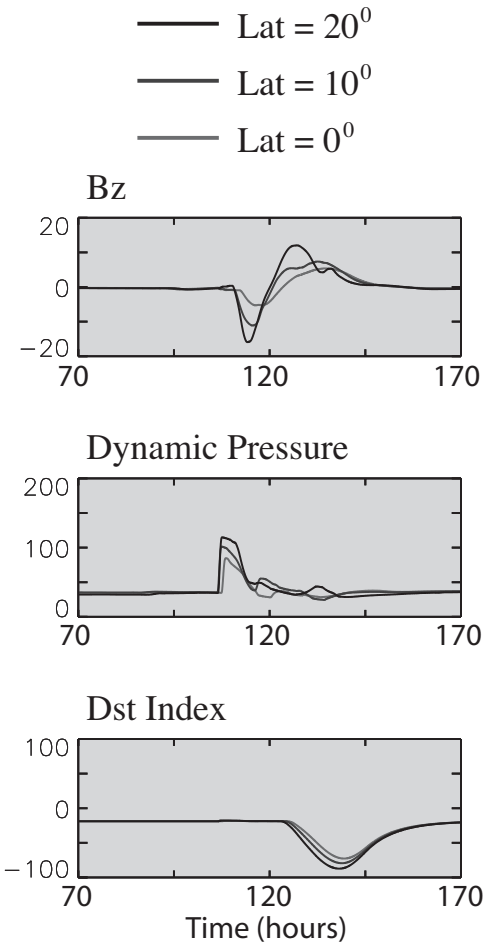

Fig. 9. Simulated profiles of several space-weather related parameters for several heliographic latitudes. From top to bottom: The z component of the IMF (B_z); the dynamic pressure; and the D_{st} index.

trailing regions of most CMEs do not apparently exhibit such velocity enhancements, we hasten to add that this does not invalidate the applicability of this, or other mechanisms to the vast majority of flux-rope CMEs.

C. Space Weather and Geo-Effective Parameters

As a final example, we can use the simulations to infer geo-effective parameters in the vicinity of Earth. In particular, by placing a hypothetical spacecraft at 1 AU in the ecliptic plane, we can derive timeseries of velocity, magnetic field, temperature, and density. From these we can construct parameters that are relevant to space weather applications, including the southward component of the interplanetary magnetic field, the solar wind dynamic pressure, and the geomagnetic Dst index (or at least that component of Dst that results from the injected ring current). In Figure 9 we show these parameters for the 2-D simulation described above. Dst was computed using a modified form of the formula derived by Burton et al. [45] (http://sprg.ssl.berkeley.edu/dst_index/estimate.html) and relies on the solar wind dawn-dusk electric field and dynamic pressure.

As part of the NSF CISM (Center for Integrated Space Weather Modeling) project, we are providing these kinds of inputs to drive magnetospheric models, effectively coupling 3 global MHD models (i.e., solar, heliospheric, and magnetospheric). Ultimately, one of the goals of this work is to predict geo-effective phenomena from self-consistent models all the way from the Sun to Earth.

VI. Summary and Future Directions

In this report we have summarized a technique for numerically modeling the eruption and evolution of CMEs from the solar surface to the vicinity of Earth. These simulations represent an inexpensive virtual laboratory, allowing us to explore a variety of solar conditions as well as probing regions of space that are not easily accessible. The solutions aid in the interpretation of complex multi-spacecraft in situ observations of interplanetary CMEs and help predict and subsequently detect new phenomena in the observations.

Predicting the path of future research is clearly speculation, undoubtedly driven, at least in part, by our current interests. Nevertheless, it may be of some use to list several topics that will likely be pursued in the upcoming years.

One challenge will undoubtedly be to develop the ability to self-consistently model CMEs with a range of properties. How do we initiate slow and fast CMEs, for example? Are they generated by the same mechanism, or are there two

(or more) mechanisms that are responsible? Self-consistent models currently can only produce flux-rope CMEs. What are the underlying differences between these and CMEs that don't contain a flux rope? Is it an observational selection effect or are there intrinsically different mechanisms for producing each type?

We may soon be entering a new era of CME modeling. In the future, our models should be increasingly capable of simulating specific events. This will require capabilities that can accurately reproduce a disparate set of remote and solar observations. To achieve these goals requires improvements in several areas: incorporating better physical concepts into the model (e.g., improved treatment of the energy equation); developing more sophisticated algorithms and codes (e.g., use of the Message Passing Interface (MPI) to make use of massively parallel architectures); and utilizing faster computers as they become available. Ultimately, their combined effect will allow us to produce an operational tool, which we believe will be capable of predicting geo-effective phenomena with up to 4 days advance warning.

ACKNOWLEDGMENT

The authors are grateful to NASA (LWS and SECTP programs) and NSF (the SHINE program and the Center for Integrated Space Weather Modeling (ATM-0120950)) for support in undertaking this work. We also thank the San Diego Supercomputer Center and the National Energy Research Supercomputer Center for providing computational support.

REFERENCES

[1] A. J. Hundhausen, "The origin and propagation of coronal mass ejections (r)," in *Sixth International Solar Wind Conference, Proceedings of the conference held 23-28 August, 1987*, V. J. Pizzo, T. E. Holzer, and D. G. Sime, Eds., vol. 2, at YMCA Technical Note Natl. Cent. for Atmos. Res., Boulder, Colo., 1987, p. 181, tech. Note TN-306.

[2] J. T. Gosling, S. J. Bame, D. J. McComas, J. L. Phillips, V. J. Pizzo, B. E. Goldstein, and M. Neugebauer, "Latitudinal variation of solar wind corotating stream interaction regions: Ulysses," *Geophys. Res. Lett.*, vol. 20, no. 24, p. 2789, 1993.

[3] J. T. Gosling, "Coronal mass ejections: An overview," vol. 99. Washington, DC: AGU, 1997, p. 9.

[4] N. U. Crooker and E. W. Cliver, "Postmodern view of m-regions," *J. Geophys. Res.*, vol. 99, no. A12, p. 23383, 1994.

[5] P. Riley, J. T. Gosling, and V. J. Pizzo, "A two-dimensional simulation of the radial and latitudinal evolution of a solar wind disturbance driven by a fast, high-pressure coronal mass ejection," *J. Geophys. Res.*, vol. 102, no. A7, p. 14677, 1997.

[6] P. Riley and J. T. Gosling, "Do coronal mass ejections implode in the solar wind?" *Geophys. Res. Lett.*, vol. 25, no. 9, p. 1529, 1998.

[7] P. Riley, "Cme dynamics in a structured solar wind," in *Solar Wind Nine Proceedings of the Ninth International Solar Wind Conference*, S. R. Habbal, R. Esser, V. Hollweg, and P. A. Isenberg, Eds., vol. 471. Nantucket, MA: The American Institute of Physics (AIP Conference Proceedings), 1999, p. 131.

[8] D. Odstrcil and V. J. Pizzo, "Three-dimensional propagation of coronal mass ejections in a structured solar wind flow, 1, cme launched within the streamer belt," *J. Geophys. Res.*, vol. 104, no. A1, p. 483, 1999.

[9] ——, "Three-dimensional propagation of coronal mass ejections in a structured solar wind flow, 2 cme launched adjacent to the streamer belt," *J. Geophys. Res.*, vol. 104, no. A1, p. 493, 1999.

[10] C. P. T. Groth, D. L. de Zeeuw, T. I. Gombosi, and K. G. Powell, "Three-dimensional mhd simulations of coronal mass ejections," *Adv. Space Res.*, vol. 26, no. 5, p. 793, 2000.

[11] W. B. Manchester, I. Roussev, M. Opher, T. I. Gombosi, D. DeZeeuw, G. Toth, I. Sokolov, and K. Powell, "3d mhd simulations of flux rope driven cmes," in *American Geophysical Union, Fall Meeting 2002*. San Francisco, CA: AGU, 2002, p. abstract SH21A.

[12] D. Odstrcil, J. A. Linker, R. Lionello, Z. Mikić, P. Riley, V. J. Pizzo, and J. G. Luhmann, "Merging of coronal and heliospheric numerical 2-d mhd models," *J. Geophys. Res.*, vol. 107, no. A12, p. abstract SSH 14, 2002.

[13] Z. Mikić and J. A. Linker, "Disruption of coronal magnetic field arcades," *Astrophys. J.*, vol. 430, no. 2/1, p. 898, 1994.

[14] R. Lionello, Z. Mikić, and J. A. Linker, "Magnetohydrodynamics of solar coronal plasmas in cylindrical geometry," *J. Comput. Phys.*, vol. 140, p. 172, 1998.

[15] Z. Mikić, J. A. Linker, D. D. Schnack, R. Lionello, and A. Tarditi, "Magnetohydrodynamic modeling of the global solar corona," *Phys. Plasmas*, vol. 6, no. 5, p. 2217, 1999.

[16] D. Odstrcil, "Interactions of solar wind streams and related small structures," *J. Geophys. Res.*, vol. 99, no. A9, p. 17653, 1994.

[17] G. Toth and D. Odstrcil, "Comparison of some flux corrected transport and total variation diminishing numerical schemes for hydrodynamic and magnetohydrodynamic problems," *J. Comput. Phys.*, vol. 128, p. 82, 1996.

[18] R. Lionello, Z. Mikić, and J. A. Linker, "Stability of algorithms for waves with large flows," *J. Comp. Phys.*, vol. 152, no. 1, p. 346, 1999.

[19] J. A. Linker, Z. Mikić, D. A. Bisecker, R. J. Forsyth, S. E. Gibson, A. J. Lazarus, A. Lecinski, P. Riley, A. Szabo, and B. J. Thompson, "Magnetohydrodynamic modeling of the solar corona during whole sun month," *J. Geophys. Res.*, vol. 104, no. A5, p. 9809, 1999.

[20] D. E. Billings, *A Guide to the Solar Corona*. New York: Academic Press, 1966.

[21] J. A. Linker and Z. Mikić, "Disruption of a helmet streamer by photospheric shear," *Astrophys. J., Part 2 - Letters*, vol. 438, no. 1, p. L45, 1995.

[22] D. J. McComas, J. T. Gosling, and R. M. Skoug, "Ulysses observations of the irregularly structured mid-latitude solar wind during the approach to solar maximum," *Geophys. Res. Lett.*, vol. 27, no. 16, p. 2437, 2000.

[23] T. G. Forbes, "A review on the genesis of coronal mass ejections," *J. Geophys. Res.*, vol. 105, no. A10, p. 23153, 2000.

[24] Z. Mikić, D. C. Barnes, and D. D. Schnack, "Dynamical evolution of a solar coronal magnetic field arcade," *Astrophys. J.*, vol. 328, no. Part 1, p. 830, 1988.

[25] J. A. Linker and Z. Mikić, "Extending coronal models to earth orbit," *Coronal Mass Ejections*, vol. 99, p. 269, 1997, edited by N. Crooker, J. Joselyn, and J. Feynmann, p. 269, AGU, Washington, D. C.

[26] T. Amari, T. Boulmezaoud, and Z. Mikić, "An interactive method for the reconstruction break of the solar coronal magnetic field. 1. method for regular solutions," *Astron. Astrophys.*, vol. 350, p. 1051, 1999.

[27] T. Amari, J. F. Lucini, Z. Mikić, and J. A. Linker, "A twisted flux rope model for coronal mass ejections and two-ribbon flares," *Astrophys. J.*, vol. 529, no. 1, p. L49, 2000.

[28] J. A. Linker, R. Lionello, Z. Mikić, and T. Amari, "Magnetohydrodynamic modeling of prominence formation within a helmet streamer," *J. Geophys. Res.*, vol. 106, no. A11, p. 25165, 2001.

[29] D. F. Webb, J. Burkepile, T. G. Forbes, and P. Riley, "Observational evidence of new current sheets within cmes," *Accepted for publication in J. Geophys. Res.*, 2003.

[30] D. Odstrcil, M. Dryer, and Z. Smith, "Propagation of an interplanetary shock along the heliospheric plasma sheet," *J. Geophys. Res.*, vol. 101, no. A9, p. 19973, 1996.

[31] J. Newkirk, G., A. J. Hundhausen, and V. J. Pizzo, "Solar cycle modulation of galactic cosmic rays - speculation on the role of coronal transients," *J. Geophys. Res.*, vol. 86, p. 5387, 1981.

[32] J. T. Gosling, D. N. Baker, S. J. Bame, W. C. Feldman, R. D. Zwickl, and E. J. Smith, "Bidirectional solar wind electron heat flux events," *J. Geophys. Res.*, vol. 92, p. 8519, 1987.

[33] J. T. Gosling, J. Birn, and M. Hesse, "Three-dimensional magnetic reconnection and the magnetic topology of coronal mass ejection events," *Geophys. Res. Lett.*, vol. 22, no. 8, p. 869, 1995.

[34] D. Lario, D. K. Haggerty, E. C. Roelof, S. J. Tappin, R. J. Forsyth, and J. T. Gosling, "Joint ulysses and ace observations of a magnetic cloud and the associated solar energetic particle event," *Space Sci. Rev.*, vol. 97, no. 1/4, p. 277, 2001.

[35] P. Riley, J. A. Linker, Z. Mikić, D. Odstrcil, T. H. Zurbuchen, D. A. Lario, and R. P. Lepping, "Using an mhd simulation to interpret the

global context of a coronal mass ejection observed by two spacecraft," *Accepted for publication in J. Geophys. Res.*, vol. 108, no. A7, p. abstract SSH 2, 2003.

[36] P. Riley, J. A. Linker, Z. Mikić, D. Odstrcil, V. J. Pizzo, and D. F. Webb, "Evidence of posteruption reconnection associated with coronal mass ejections in the solar wind," *Astrophys. J.*, vol. 578, no. 2, p. 972, 2002.

[37] P. A. Sweet, *Nuovo Cimento Suppl.*, vol. 8, p. 188, 1958.

[38] ——, "The neutral point theory of solar flares," *IAU Symp., 6 Electromagnetic Phenomena in Cosmical Physics*, p. 123, 1958.

[39] E. N. Parker, "Interplanetary dynamical processes," *New York, Interscience Publishers*, 1963.

[40] H. E. Petschek, "The physics of solar flares," W. N. Hess, Ed., vol. SP-50. (NASA SP-50; Washington, D. C.: NASA): in Proc. AAS-NASA Symp., 1964, p. 425.

[41] L. W. Klein and L. F. Burlaga, "Interplanetary magnetic clouds at 1 au," *J. Geophys. Res.*, vol. 87, p. 613, 1982.

[42] K. Marubashi, "Interplanetary magnetic flux ropes and solar filaments, in coronal mass ejections," in *Coronal Mass Ejections (Geophys. Monogr.)*, N. U. Crooker, J. A. Joselyn, and J. Feynman, Eds., vol. 99. Washington, DC: AGU, 1997, p. 147.

[43] R. P. Lepping, J. A. Jones, and L. F. Burlaga, "Magnetic field structure of interplanetary magnetic clouds at 1 au," *J. Geophys. Res.*, vol. 95, p. 11957, 1990.

[44] S. K. Antiochos, "The magnetic topology of solar eruptions," *Astrophys. J. Ltrs.*, vol. 502, p. L181, 1998.

[45] R. K. Burton, R. L. McPherron, and C. T. Russell, "An empirical relationship between interplanetary conditions and dst," *J. Geophys. Res.*, vol. 80, p. 4204, 1975.